Further insight into the microstructure of compacted bentonite-sand mixture

S. Saba, Pierre Delage, N. Lenoir, Yu-Jun Cui, Anh Minh A.M. Tang, Jean-Dominique Barnichon

Further insight into the microstructure of compacted bentonite-sand mixture

Simona Saba[1,2], Pierre Delage[1], Nicolas Lenoir[1], Yu Jun Cui[1], Anh Minh Tang[1], Jean-Dominique Barnichon[2]

[1]Ecole des ponts ParisTech, Navier/CERMES, Université Paris-Est
[2]Institut de Radioprotection et Sûreté Nucléaire - IRSN

Corresponding author:

Pr. Pierre DELAGE

Ecole des Ponts ParisTech
6-8 avenue Blaise Pascal
F 77455 MARNE-LA-VALLEE cdx 2
France

Email : delage@cermes.enpc.fr
33 1 64 15 35 42

Abstract

Compacted bricks of bentonite/sand mixture are planned to be used as sealing plugs in deep radioactive waste disposal repositories because of their low permeability, high swelling capacity and favourable properties with respect to radionuclide retention. The isolating capacity of compacted bentonite/sand mixture is closely related to microstructure features that have been often investigated, in particular by using scanning electron microscope (SEM or ESEM) and mercury intrusion porosimetry (MIP).

In this work, microfocus X-ray computed tomography (μCT) observations were used in parallel with MIP measurements to further investigate at larger scale the microstructure of a laboratory compacted bentonite/sand disk (65/35% in mass). Qualitative observation of μCT images showed that sand grains were inter-connected with some large pores between them that were clearly identified in the bimodal pore distribution obtained from MIP measurements. Due to gravitational and to frictional effects along the specimen periphery, a higher density was observed in the centre of the specimen with bentonite grains more closely compacted together. This porosity heterogeneity was qualitatively estimated by means of image analysis that also allowed the definition of the representative elementary volume. Image analysis also provided an estimation of the large porosity in good agreement with MIP measurements.

Keywords: compacted sand-bentonite mixture, sealing plug, radioactive waste disposal, microstructure, mercury intrusion porosimetry, X ray micro tomography

Introduction

In deep radioactive waste disposal concepts, sealing plugs made of compacted bentonite/sand blocks are planned to be used to close the galleries and to limit water transfers. Compacted bentonite/sand plugs are used for their low permeability, high radionuclides retention capability and sealing/swelling abilities when infiltrated by water (e.g. Pusch, 1979; Yong et al., 1986). Once the disposal galleries are closed, plugs will be progressively infiltrated by the pore water of the host rock. They will swell and seal the so-called technical voids of the system, i.e. the voids remaining between blocks and at the interfaces with the rock. These technical voids are estimated at 14% of the total volume of the plugs by IRSN (Institut de Radioprotection et de Sûreté Nucléaire, the French expert Institution in the field of nuclear safety) in the in-situ SEALEX experiment that they carry out in their Tournemire Underground Research Laboratory.

Various investigations of the microstructure of compacted bentonites and sand bentonite mixture have been carried out by using mercury intrusion porosimetry (MIP) and scanning electron microscopy (SEM, ESEM, Komine and Ogata, 1999; Villar and Lloret, 2001; Montes-H, 2002; Cui et al., 2002; Lloret et al., 2003; Agus and Schanz, 2005; Delage et al., 2006). These techniques require a cautious preliminary dehydration of the samples, most often by freeze-drying. They provide local observations on a small part of millimetric samples. These localized analytical techniques can be fruitfully complemented by use of by microfocus X-ray computed tomography (μCT), a high-resolution non destructive 3D observation technique. The μCT does not need any

77 sample pre-treatment and gives further 3D information on the whole sample (including
78 grain size distribution as well as pore size distribution and pore inter-connectivity).
79 Previous applications of μCT have been devoted to the monitoring of hydro-chemo-
80 mechanical processes (Comina et al., 2008), to the detection of dessication cracks
81 (Gerbrenegus et al., 2006; Mukunoki et al., 2006), to the visualisation of
82 diffusion/hydration phenomena, to the study of fluid movements (Rolland et al., 2003;
83 Rolland et al., 2005; Carminati et al., 2006; Koliji et al., 2006) and to the investigation
84 of the microstructure of compacted bentonite based materials (Kozaki et al., 2001, Van
85 Geet et al., 2005 and Kawaragi et al., 2009). In this work, μCT was coupled to MIP for
86 further microscopic investigation of a compacted bentonite/sand sample.

87 # Material and methods

88 ## *Material*

89 The studied material is a compacted mixture of Wyoming MX-80 bentonite (65% in dry
90 mass, commercial name Gelclay WH2) and sand (35%). The MX80 bentonite contains
91 92% of montmorillonite with several other minerals including quartz, alumina, and
92 hematite (Tang et al., 2008). The sand is quartz sand (commercial name TH1000).
93
94 The sand-bentonite mixture was provided in boxes containing a powder with an initial
95 water content of 10.2% and a suction of 73.3 MPa measured with a chilled mirror dew
96 point tensiometer (Decagon WP4). Samples of sand and bentonite were also provided
97 separately. The grain size distribution of the bentonite powder obtained by dry sieving
98 is presented in Figure 1 together with that of the deflocculated bentonite obtained by
99 sedimentation. The grain size distribution of the sand is also plotted in Figure 1.

The grain size distribution curves show that the bentonite powder grains are larger than the sand grains with D_{50} values of 1.2 and 0.6 mm respectively. Both curves are representative of well sorted materials. The unit mass of the bentonite particles that constitute the bentonite grains was measured by using a pycnometer with water and was found equal to 2.77 Mg/m^3 in agreement with published data (Madsen, 1998; Karnland et al., 2006). The unit mass of the bentonite powder was determined by using a pycnometer with a non aromatic hydrocarbon fluid (commercial name Kerdane). The bentonite grains appeared to be stable once immersed in Kerdane and a value of 2 Mg/m^3 was obtained. This value could suffer from some uncertainty due to possible Kerdane infiltration into the grains. A comparable unit mass value was however obtained from the cumulative pore size distribution curve presented later in Figure 2 that allows determining the unit mass of the bentonite grains from the value of inter-grains porosity. The unit mass of the sand grains was found equal to 2.65 Mg/m^3.

Compacted samples were prepared by uniaxial static compaction (strain rate of 0.1 mm/min) in a cylindrical mould in order to obtain a disk (diameter 50 mm, height 10 mm) at the targeted dry density (1.8 Mg/m^3 obtained at a maximum compaction stress of 25.5 MPa). The sample water content was 10%, resulting in a degree of saturation of 55 % and a suction of 76.3 MPa. Note that this value is close to that of the powder prior to compaction (73.3 MPa). The slightly higher value could be due to some effects of evaporation during the process of compaction. In any case, these small changes in suction after compaction are consistent with the observations of Li (1995), Gens et al. (1995) and Tarantino and De Col (2008) on soils compacted on the dry side of Proctor

124 optimum. It confirms that suction is governed by aggregates that are not much affected
125 by the compaction. As a consequence, there is little dependency of the water retention
126 properties on the sample density in compacted bentonite based materials.

127 *Mercury intrusion porosimetry*

128 The pore size distribution of the compacted samples was measured on freeze dried
129 samples by using an Autopore IV 9500 mercury intrusion porosimeter (Micromeritics)
130 working to a maximum pressure of 230 MPa. Instantaneous freezing was carried out by
131 plunging small samples (volume 0.40 cm^3) into slush nitrogen (liquid nitrogen at cooled
132 down from -195°C to -210°C by vacuum application, Delage et al., 2006). In such
133 conditions, there is no nitrogen boiling around the samples when plunging them into
134 nitrogen, resulting in an optimized quick freezing and good microstructure preservation.
135 The intruded porosity was determined from the total volume of mercury intruded into
136 the sample and the pore size distribution was obtained, in a standard fashion, assuming
137 parallel, cylindrical nonintersecting pores of different radii, using the Autopore IV 9500
138 V1.09 standard software package. The intruded porosity was systematically compared
139 to the total porosity obtained by standard methods so as to detect the smaller porosity
140 (entrance equivalent diameter smaller than 5.5 nm) not intruded by mercury at the
141 highest applied pressure (200 MPa).

142 *Microfocus X-ray tomography and image analysis*

143 Microfocus x-ray computed tomography (μCT) was used to examine in three
144 dimensions the internal microstructure of the compacted bentonite/sand mixtures. μCT
145 is a non-destructive observation technique that has proven to be useful in the
146 investigation of various geological porous media including compacted bentonite

147 (Kozaki et al., 2001), bentonite pellet/powder mixture (Van Geet et al., 2005) and
148 compacted bentonite/quartz mixture (Kawaragi et al., 2009). µCT consists firstly of
149 recording a set of two-dimensional X-ray radiographs of an object at several angles
150 (typically at 180° or 360°) and secondly in reconstructing the 3D slices from the
151 radiographs using a mathematical algorithm. The final 3D image of the internal
152 structure is obtained by stacking the slices. The final measurement is the attenuation
153 coefficient to x-ray which depends on the mass density and the atomic number of the
154 object (Ketcham and Carlson, 2001; Van Geet et al., 2005).
155
156 The µCT scans presented here were carried out with the device of the Navier laboratory
157 (Ecole des Ponts ParisTech), an "Ultratom" device specifically designed and
158 manufactured by RXsolutions (France). Images were reconstructed using the software
159 Xact-reconstruction developed by RXsolutions. The system is a dual-head and dual-
160 imager scanner; two sources [a nano-focus xs-160hpnf/GE-Phoenix (160 kV, 15W, 0.9
161 µm min spot size) and a micro-focus xs-225d/GE-Phoenix (225 kV, 320W, 5 µm min
162 spot size)], two interchangeable imagers: [HD camera PhotonicScience VHR
163 (4008x2672 pixels, 9µm pixel size) and a flat-panel-CsI scintillator-Varian
164 2520V/Paxscan (14 bit, 1920x1526 pixels, 127µm pixel size)].
165
166 A micro-focus source was used together with a flat panel. The X-ray source parameters
167 were a voltage of 140 kV with an intensity of 210 µA, a source power resulting in a spot
168 size below or equal to the spatial resolution, here a voxel size of 30 µm (a voxel
169 describes a Volume Pixel which is the smallest distinguishable box-shaped portion of a
170 three-dimensional image). The sample was scanned using 1440 projections on 360°

171 with an exposure time of 0.2 s. Each projection was integrated on 4 s (average of 20
172 frames) in order to obtain a good signal-to-noise ratio. The total scanning time was
173 about an hour and a half. The final 3D image is a 16 bit type with a size of
174 1840x1840x386 voxels. The image analysis and treatment was then carried out by using
175 ImageJ, a public domain Java image processing program (Rasband, 1997-2012). Note
176 that the image was first converted to 8 bit for size reasons.

177 Results

178 *Pore size distribution*

179 The pore size distribution determined at a dry density of 1.8 Mg/m^3, a water content of
180 10% and a suction of 76.6 MPa is presented in terms of cumulative and density
181 functions curves in Figure 2. The bimodal curve obtained is comparable to that of
182 samples compacted dry of optimum (Ahmed et al., 1974; Delage et al., 1996; Romero et
183 al., 1999 among others) and also with the results of Cui et al. (2002), Lloret et al.
184 (2003), Agus and Schanz, (2005) on compacted bentonite materials. The PSD curve
185 indicates that the smaller pores population (micropores) has a mean entrance diameter
186 of 0.19 μm and the larger pore population (macro-pores) has a mean entrance diameter
187 of 22 μm. Note that the intrusion of mercury into the specimen starts at quite a low
188 pressure, evidencing a largest diameter of 360 μm, the upper limit of the method. The
189 total porosity (0.337) calculated in a standard fashion by macroscopic volume
190 measurements is also plotted in Figure 2. The smaller value of the porosity intruded by
191 mercury (0.273) confirms that pores with an entrance diameter smaller than 5.5 nm (the
192 lower limit of MIP) could not be intruded by mercury. This feature is typical of

compacted bentonites and strongly depends on the water content (the higher the water content, the higher the smallest porosity, see Delage et al., 2006).

Microfocus X-ray computed tomography (µCT)

Image Observation

The reconstructed 3D volume of a compacted sample of bentonite/sand mixture at a dry density of 1.8 Mg/m^3 and a water content of 10% is presented in Figure 3. The position of the plane where the cross section has been done is indicated. The horizontal cross section at 4 mm from the top of the sample is provided in Figure 4.

The µCT technique is able to distinguish the various components according to their density and atomic composition (the grey level range goes from white representing high attenuating material to black representing void). A clear distinction can be made between the clearer sand grains and the less clear larger bentonite powder grains (hydrated at a gravimetric water content of 10.6%), even though their respective densities are not so different (around 2 Mg/m^3 for the bentonite grains and 2.65 Mg/m^3 for sand grains). This is due to the atomic composition difference. One can also observe in Figure 4 that the sample density is not strictly homogeneous with more voids observed around the sample and a larger density with less voids in the centre. This shows that, unsurprisingly, compaction was less effective around the sample along the ring against which friction effects resulted in looser compaction. Detailed observation made on a zoom taken close to the sample perimeter also shows that the bentonite powder grains remain clearly apparent around the sample and that they are apparently

more frequent than in the centre. In the centre, powder grains appear to be more compacted one against another, resulting in a denser structure.

Inspection of Figure 4 also shows that the bentonite/sand mixture is not really homogeneous and that sand grains and powder grains appear to be somewhat segregated. As indicated in the Figure, aggregations of powder grains are observed in some locations and sand grain packings with inter-grains pores in other locations. This segregation, probably resulting from the difference in density between the bentonite powder and the sand grains, is not compatible with the common statement that, in a 35-65% sand/bentonite mixture, sand grains should be homogeneously scattered among a (supposedly finer) clay matrix. Conversely, it seems that, due to segregation, some continuity between the sand grains is observed. As a consequence, there could be some continuity and interconnection of the pores located between sand grains.

Note that this segregation is probably depending on the process adopted here of pouring the dry mixture into the ring. It would hence be interesting to investigate the effects of two possible options for preparing more homogeneous sand-bentonite mixture: i) by previously moisturizing the mixture so as to make the clay grains stick to sand particles, resulting in less segregation than in the dry mixture, provided the wet mixture is thoroughly mixed prior to being poured into the ring and ii) by grinding bentonite grains to smaller sizes. Obviously, the heterogeneity observed here is typical of the preparation procedure of pouring a dry mixture into the compaction ring.

239 A more detailed examination of the voids configuration shows that many voids are
240 located between sand grains. Around the sample, some voids are also located between
241 powder grains but this is less true in the denser centre in which bentonite grains appear
242 to be aggregated together. This means that the maximum compression stress, in spite of
243 being as high as 25.5 MPa, is not high enough to allow the intrusion of clay particles
244 (hydrated at a water content of 14.5 % with a 76.6 MPa suction) into the pores located
245 between the sand grains. This high compression stress only allows some aggregation of
246 bentonite grains as observed in the centre (around 8 grains of various diameters are
247 aggregated in the circle indicated). This slight deformability of dry grains under high
248 stresses is compatible with the observation made above about the small suction
249 variations observed when compacting samples in dry conditions: compaction affects the
250 assembly of bentonite grains but not significantly the bentonite grains themselves, the
251 microstructure of which is governing suction.
252
253 Visual observation of two cross sections close to the bottom and to the top of the sample
254 also showed that the pore distribution was not homogeneous along the axial direction,
255 with more large pores and large particles observed in the bottom of the sample. This is
256 related to segregation effects during sample preparation. When pouring the powder into
257 the compaction mould, the largest grains first tumble resulting in more macropores at
258 the bottom. Indeed, this problem could be solved by using wet mixture with bentonite
259 grains sticking along sand grains and then reducing segregation.
260
261 Figure 4 provides further information about the interpretation of the PSD curves
262 provided in Figure 2, in which one observes that mercury intrusion started in

macropores with an entrance diameteras large as 330 μm and an average diameter of the corresponding pore population equal to 22 μm. This size is compatible with the inter-grain pores observed in μCT in Figure 3. Given that the sample tested by MIP was extracted from the specimen centre where bentonite grains are more closely compacted together, this pore population is mainly related to the pores located between the sand grains. The clear presence of the pore inter-grains population in the PSD curve confirms the interconnection of inter-grains pores along the grain skeleton that was suspected from the μCT image and commented above. Hence, the bimodal porosity that is generally related to inter-aggregate and intra-aggregate pores in soils compacted dry of optimum (Ahmed et al 1974, Delage et al. 1996, Romero et al. 1999) is due here to the nature of the mutual arrangement of sand and bentonite powder grains. Indeed, the inter-aggregate average entrance pore diameter observed by Delage et al. (1996) in a compacted low plasticity Jossigny silt is 8 μm whereas Romero et al. (1999) detected inter-aggregates pores close to 2 μm in compacted Boom clay. The significantly larger average entrance pore diameter detected here is too large to be representative of inter-aggregate pores as in the case of standard compacted soils. It is linked to the connected inter-grains pores observed along the sand skeleton in μCT.

Image analysis

Further investigation of the microstructure was carried out by using the ImageJ image analysis software. The first step was to reduce noise by applying a 3D median filter with a 1 pixel radius. Then, a segmentation of the image is needed in order to isolate pores from the other existing phases. The choice of the threshold value is made by using the "mixture modelling" plug in. The mixture modelling technique is a histogram based technique that assumes that the histogram distribution is represented by two Gaussian

287 curves. The histogram is then separated in two classes using a Gaussian model and a
288 threshold value of 73 is then calculated as the intersection of the two Gaussians. Figure
289 5 shows the histogram of the image on a linear (black) and logarithmic (grey) scale. The
290 linear graph doesn't exhibit two clearly distinct peaks because the number of pore's
291 voxels is too small compared to that of the grains. However the logarithmic graph
292 evidences a non-symmetrical shape that indicates the presence of the smaller pore
293 population. The two Gaussians are then fitted using the "mixture modelling" plug in as
294 seen in the Figure 5 represented by the white (continuous and dashed) curves.
295
296 Figure 6 shows an image at different stages before segmentation: a) initial state; b) after
297 applying a 3D median filter; c) after applying a 73 threshold value (Figure 5) and d) the
298 segmented image. An investigation on the effect of the size of the studied volume on the
299 calculated porosity was done. To do so, the porosity was calculated by using the
300 histogram of the segmented image and by dividing the number of black voxels by the
301 total number of voxels. Starting from the middle horizontal cross section of the sample
302 at different positions (see Figure 7a), cubic volumes were selected with sides starting
303 from 21 to 271 pixels. The side on the *z* direction is limited by the height of the sample
304 (10 mm) that corresponds to a maximum thickness of 271 pixels. *x* and *y* were
305 afterwards increased until 700 resulting in a parallelepiped volume. The porosity values
306 calculated with respect to the considered volumes are plotted in Figure 7. The curves
307 start with some irregularities and then stabilise. Some curves continuously and slowly
308 increase (bottom and right in Figure 7a). These increases suggest a spatial heterogeneity
309 of the porosity. Indeed, when the studied volume increases, porosity increases because
310 some zones located on the side of the specimen with higher porosity are more and more

311 included into the volume. Stabilization is observed for volumes greater than 20 x 10^6
312 voxels. This volume corresponds to a cube with a side approximately equal to the height
313 specimen i.e. 271 pixels. It can hence be considered as a Representative Elementary
314 Volume (REV). This side size corresponds to 9 adjacent grains (D_{50} mixture = 0.9 mm
315 = 30 voxels) in accordance with previous studies (e.g. Razavi et al., 2007).
316
317 The spatial distribution of the porosity is now investigated at different locations along
318 the *x* and *y* directions by using volumes with heights equal to 271 pixels. The locations
319 of the volumes sections investigated are presented in Figure 8. Figure 9 shows the
320 variation of porosity with respect to *x* and *y* (volumes 1 to 12 in Figure 8). A clear
321 difference is observed in the porosity values between the border (*x*, *y* = 160 and 1515)
322 and the centre. A significant difference in porosities is also noticed for *x* (or *y*) varying
323 between 1244 and 1515 while *y* (or *x*) equals 925. It corresponds to cubes 5 and 6, 11
324 and 12 in Figure 8. The porosity variation at these points is not smooth like in the others
325 but the slope is steep showing a sudden change in porosity. It confirms the slow
326 increase observed in the REV study (Figure 7b), since it corresponds to the same
327 positions (right for cubes 5 and 6 and bottom for cubes 11 and 12).
328
329 The same study is now made on concentric rings having a height of 271 pixels and a
330 width of 167 pixels starting from the centre (radius from 0 to 167) to the contour (radius
331 from 501 to 835, see Figure 10).
332
333 The porosities obtained with respect to the radius are presented in Figure 11. The
334 smallest detail that can be identified in the μCT images is defined by the size of the

voxel (30 μm). The porosity estimated by image analysis only concerns pores with a diameter larger than 3 voxels (partial volume effect). The value of the cumulated porosity of pores larger than 90 μm from the PSD curves (Figure 2) is 0.0108. This value is in the same range as that obtained by image analysis in the central part of the sample where MIP was performed (0.0135 porosity for radius smaller or equal to 334 voxels). This confirms that, in spite of some limitation related to the voxel size, μCT is an interesting complementary method to MIP for estimating the macropores and giving additional information on the spatial distribution of the porosity.

Discussion

Most of the investigations carried out up to now on compacted soils in laboratory have been obtained from the combined use of MIP and SEM on freeze dried samples. It is commonly accepted that the bimodal pore distribution observed in fine-grained soils compacted dry of optimum is due to the aggregate microstructure of compacted soils, with macro-pores being inter-aggregate pores and micropores being intra-aggregate pores (Ahmed et al. 1974, Delage et al. 1996). In such soils, it has also been demonstrated that compaction has little effect on the sample's suction (Li et al., 1995, Gens et al., 1995, Tarantino and De Col, 2009), given that suction is governed by intra-aggregate phenomena (mainly the adsorption of water in the clay fraction, Romero et al., 1999) whereas the change in density are due to the compression of larger inter-aggregate pores with little effect on the aggregates (Delage, 2009).

Compacted bentonites and sand-bentonite mixtures are a special case of compacted soils. They are obtained by compacting powder grains that may have, as observed here,

358 a size significantly larger than the aggregates in laboratory compacted soils. Compacted
359 bentonites and sand-bentonite mixtures also have quite large values of suction
360 (76.6 MPa here). In the mixture studied here, the powder grains of bentonite (1.2 mm
361 average diameter) are larger than the sand grains (0.6 mm average diameter). As in
362 standard compacted soils, suction appeared here not to change significantly before and
363 after compaction (73.3 MPa in the powder before and 76.6 MPa after compaction),
364 confirming a well known trend in compacted soils.
365
366 Compared to MIP and SEM, μCT provided more information on the larger scale
367 structure, going from the size of the grains (sand and bentonite, 1 mm order of
368 magnitude) to the size of the specimen (50 mm), i.e. on a scale much larger and more
369 representative than both MIP and SEM. Interestingly, μCT has been able to distinguish
370 clearly enough the bentonite from the sand grains within the compacted mixture, in
371 spite of small difference in density. Thus, μCT provided interesting complements to
372 MIP and SEM observations, including granules connectivity and distribution through
373 the sample.
374
375 An important point is that μCT observation confirmed that the bentonite grains seem to
376 have not been crushed during compression. They still have an average size compatible
377 with macroscopic grain size measurements and an angular shape with no clear
378 appearance of local grain breakage. This finding is in agreement with the small variation
379 of suction before and after compaction, as suspected from studies in laboratory
380 compacted soils. Suction didn't change because the grains have not been significantly
381 affected by compression, even under 25.5 MPa. μCT also provides clear information

382 about the mutual arrangement of sand and bentonite grains within the mixture, showing
383 that it is not really homogeneous with some continuity observed between sand grains
384 with the bentonite grains (65% in mass) located within the sand grains assembly (35%
385 in mass). The common hypothesis of having sand grains isolated within a clay matrix is
386 not confirmed and some continuity of the inter-grains porosity is suspected. In the
387 looser zone around the sample, some large pores with a size comparable to that of the
388 inter-grains pores have also been observed between the bentonite grains. These pores,
389 that are likely to exist in less densely compacted sand-bentonite samples, are no longer
390 observed in the denser central zone in which the compaction stress appears to be high
391 enough to aggregate the bentonite grains together.
392
393 In spite of the precautions taken during sample preparation, μCT clearly evidenced that
394 the compacted sand-bentonite mixture was heterogeneous with looser zones all around
395 the sample close to the ring in which compaction was made. This difference could have
396 been better estimated by running MIP tests at different distances from the centre to
397 compare them with the data of Figure 2 obtained in the denser central area. Some
398 segregation probably resulting from the difference in density between the bentonite and
399 the sand grains was also detected by μCT. Again, the use of a wetter mixture as
400 commented above could have helped achieving better heterogeneity with a mixture less
401 sensitive to gravity segregation effects during pouring. The heterogeneity observed is
402 certainly linked to the dry mixing preparation procedure used here and this conclusion
403 should not apply to wetter mixture. Note however that bentonite grains were at
404 equilibrium with ambient atmosphere and that this simple condition is likely to be
405 prevailing when preparing mixtures in real disposal system. Indeed, the process of

406 mixing a wetter bentonite mixture could add some complexity to the process of
407 preparing compacted mixtures.
408 The hydro-mechanical response of the sample should be somewhat influenced by this
409 heterogeneity, with mechanical parameters affected by the stronger central area and the
410 hydraulic conductivity affected by the smaller permeability around the sample.
411

412 # Conclusion

413 The μCT investigation of the microstructure of compacted bentonite/sand mixture
414 samples (65/35% respectively) provided interesting complementary features at larger
415 scale that could not have been identified by using MIP. μCT allowed further
416 observation of the mutual arrangement of bentonite and sand grains. The commonly
417 reported assumption that sand grains are present as isolated particles regularly scattered
418 within a clay matrix has not been observed. The results of this study showed that some
419 continuity could be observed between the sand grains with interconnected inter-grains
420 large pores that were also detected by MIP. Note that the large pore population
421 evidenced by MIP comprises pores located between sand grains and also between
422 bentonite grains as well, indicating some connectivity in this pore population.
423

424 A study on the effect of the size of the REV demonstrated that it was necessary to
425 consider a cubic volume with a size of 271 voxels (around 9 grains). The sample
426 heterogeneity due to compaction with a larger porosity around the sample was
427 quantified by carrying a 3D estimation of porosity by using image analysis.
428

429 The interconnection of inter-grains pores evidenced here could have some effects during
430 the hydration of the bentonite/sand mixture, at least in the vapour phase, since it could
431 facilitate the propagation of vapour within the mixture through connected inter-grains
432 pores. The question as to whether this porosity remains interconnected and not clogged
433 when bentonite grains start being hydrated remains. It could be examined by conducting
434 a similar investigation at various degrees of hydration. This complementary study could
435 also allow further understanding about achieving better heterogeneity by using wetter
436 sand bentonite mixture less prone to gravity segregation thanks to some possible
437 sticking of bentonite grains to the sand grains.

References

Agus S.S. and Schanz T. (2005). Effect of shrinking and swelling on microstructures and fabric of a compacted bentonite-sand mixture. *Proceedings of the International Conference on Problematic Soils*, Cyprus, 32, 543 – 550.

Ahmed S., Lovell C. W. and Diamond S. (1974). Pore sizes and strength of compacted clay. *J. Geotech. Eng. Div. Am. Soc. Civ. Eng.*, GT4, 407– 425.

Carminati A., Kaestner A., Hassanein R. and Koliji A. (2006). Hydraulic properties of aggregate-aggregate contacts. In: *Desrues J, Viggiani G, Bésuelle P (eds.) Advances in X ray tomography for geomaterials*. ISTE Ltd, London, UK, 325–331

Comina C., Foti S., Musso G. and Romero E. (2008). EIT oedometer: an advanced cell to monitor spatial and time variability in soil. *ASTM Geotechnical Testing Journal* 31 (5), 404–412.

Cui Y.J., Loiseau C. and Delage P. (2002). Microstructure changes of a confined swelling soil due to suction controlled hydration. *In Unsaturated soils: proceedings of the Third International Conference on Unsaturated Soils, UNSAT 2002*, 10-13 March 2002, Recife, Brazil, volume 2, 593-598.

Delage P. (2009). Compaction behaviour of clay: discussion. *Géotechnique* 59 (1), 75-76.

Delage P., Marcial D., Cui Y.J. and Ruiz X. (2006). Ageing effects in a compacted bentonite: a microstructure approach, *Géotechnique* 56(5):291–304.

Delage P., Audiguier M., Cui Y.J., and Howat M. (1996). The microstructure of a compacted silt. *Canadian Geotechnical Journal*, 33 (1): 150-158.

Gebrenegus T., Tuller M. and Muhuthan B. (2006). The application of X-ray computed tomography for characterisation of surface crack networks in bentonite-sand mixtures. In: *Desrues J, Viggiani G, Bésuelle P (eds) Advances in X-ray tomography for geomaterials*. ISTE Ltd, London, UK: 207–212

Gens A., Alonso E.E., Suriol J. and Lloret A. (1995). Effect of structure on the volumetric behaviour of a compacted soil. *Proc. 1st Int. Conf on Unsaturated Soils UNSAT' 95* 1, 83-88.

Karnland O., Olsson S. and Nilsson U. (2006). Mineralogy and sealing properties of various bentonites and smectite-rich clay material. *SKB report*.

Kawaragi C., Yoneda T., Sato T. and Kaneko K. (2009). Microstructure of saturated bentonites characterized by X-ray CT observations. *Engineering Geology* 106, 51–57

Ketcham R. A. and Carlson W. D. (2001). Acquisition, optimization and interpretation of X-ray computed tomographic imagery : applications to the geosciences. *Computers & Geosciences* Vol. 27, 381-400.

Koliji A., Carminati A., Kaestner A., Vulliet L., Laloui L., Fluehler H., Vontobel P. and Hassanein R. (2006). Experimental study of flow and deformation in aggregated soils using neutron tomography. In: *Desrues J, Viggiani G, Bésuelle P (eds). Advances in X-ray tomography for geomaterials*. ISTE Ltd, London, UK: 341–348

Komine H. and Ogata N. (1999) Experimental study on swelling characteristics of sand-bentonite mixture for nuclear waste disposal. *Soils and Foundations* 39 (2): 83-97.

481 Kozaki T., Suzuki S., Kozai N., Sato S. and Ohashi H. (2001). Observation of
482 microstructures of compacted bentonite by microfocus X-ray computerized
483 tomography (Micro-CT). *Journal of Nuclear Science Technology* 38 (8), pp. 697–699
484 Li Z.M. (1995). Compressibility and collapsibility of compacted unsaturated loessial
485 soils. *Proceedingsof the 1st International Conference on Unsaturated Soils UNSAT'*
486 *95* 1, 139-144, Paris, Balkema, Rotterdam.
487 Lloret A., Villar M.V., Sanchez M., Gens A., Pintado X. & Alonso E.E. 2003.
488 mechanical behaviour of heavily compacted bentonite under high suction changes.
489 *Géotechnique* 53 (1), 27-40.
490 Madsen FT. (1998). Clay mineralogical investigations related to nuclear waste disposal.
491 *Clay Minerals*, 33(1):109–129.
492 Montes-H G. (2002) Etude expérimentale de la sorption d'eau et du gonflement des
493 argiles par microscopie électronique à balayage environnementale (ESEM) et analyse
494 digitale d'images. *PhD Thesis*. Université Louis Pasteur, Strasbourg, France.
495 Mukunoki T., Otani J., Maekawa A., Camp S., Gourc J.P. (2006). Investigation of crack
496 behaviour on cover soils at landfill using X-ray CT. *In: Desrues J, Viggiani G,*
497 *Bésuelle P(eds) Advances in X-ray tomography for geomaterials*. ISTE Ltd, London,
498 UK: 213–219.
499 Pusch, R. (1979). Highly compacted sodium bentonite for isolating rock-deposited
500 radioactive waste products. *Nucl. Technol*, United States. 45(2):153-157.
501 Rasband W.S. (1997-2012). ImageJ, U. S. National Institutes of Health, Bethesda,
502 Maryland, USA, http://imagej.nih.gov/ij/.
503 Razavi M.R., Muhunthan B. and Al Hattamleh O. (2007) Representative elementary
504 volume analysis using X-ray computed tomography, *Geotechnical Testing Journal* 30
505 (3), 212-219.
506 Rolland S., Stemmelen D., Moyne C. and Masrouri F. (2003). Transfert hydrique dans
507 un sol argileux gonflant non saturé: influence du confinement. *Revue Française de*
508 *Géotechnique* 104, 21–35
509 Rolland S., Stemmelen D., Moyne C. and Masrouri F. (2005). Experimental hydraulic
510 measurements in an unsaturated swelling soil using the dual-energy gamma-ray
511 technique. *Proceedings of International Symposium on Advanced Experimental*
512 *Unsaturated Soil Mechanics, Trento, Italy*. In: Tarantino A, Romero E, Cui YJ (eds)
513 Advanced experimental unsaturated soil mechanics. Taylor, Francis Group, London,
514 305–310.
515 Romero E., Gens A., and Lloret A. (1999). Water permeability, water retention and
516 microstructure of unsaturated compacted Boom clay. *Engineering Geology*, 54 (1-2):
517 117-127.
518 Tang A.M., Cui Y.J. and Le T.T. (2008). A study on the thermal conductivity of
519 compacted bentonites. *Applied Clay Science*; 41 (3-4):181-189.
520 Tarantino A. and De Col E. (2008). Compaction behaviour of clay. *Géotechnique* 58
521 (3): 199-213.
522 Van Geet M., Volckaert G. and Roels S. (2005). The use of microfocus x-ray computed
523 tomography in characterising the hydration of a clay pellet/powder mixture. *Applied*
524 *Clay Science*, 29 (2):73–87, 2005.

525 Villar M.V. and Lloret A. (2001). Variation in the intrinsic permeability of expansive
526 clays upon saturation. *In: Adachi K., Fukue M. (eds) Clay Science for Engineering*.
527 *A.A. Balkema, Rotterdam*, 259-266.
528 Yong R.N., Boonsinsuk P. and Wong G. (1986). Formulation of backfill material for a
529 nuclear fuel waste disposal vault. *Canadian Geotechnical Journal*, 23(2):216–228.
530
531

532 **List of figures**

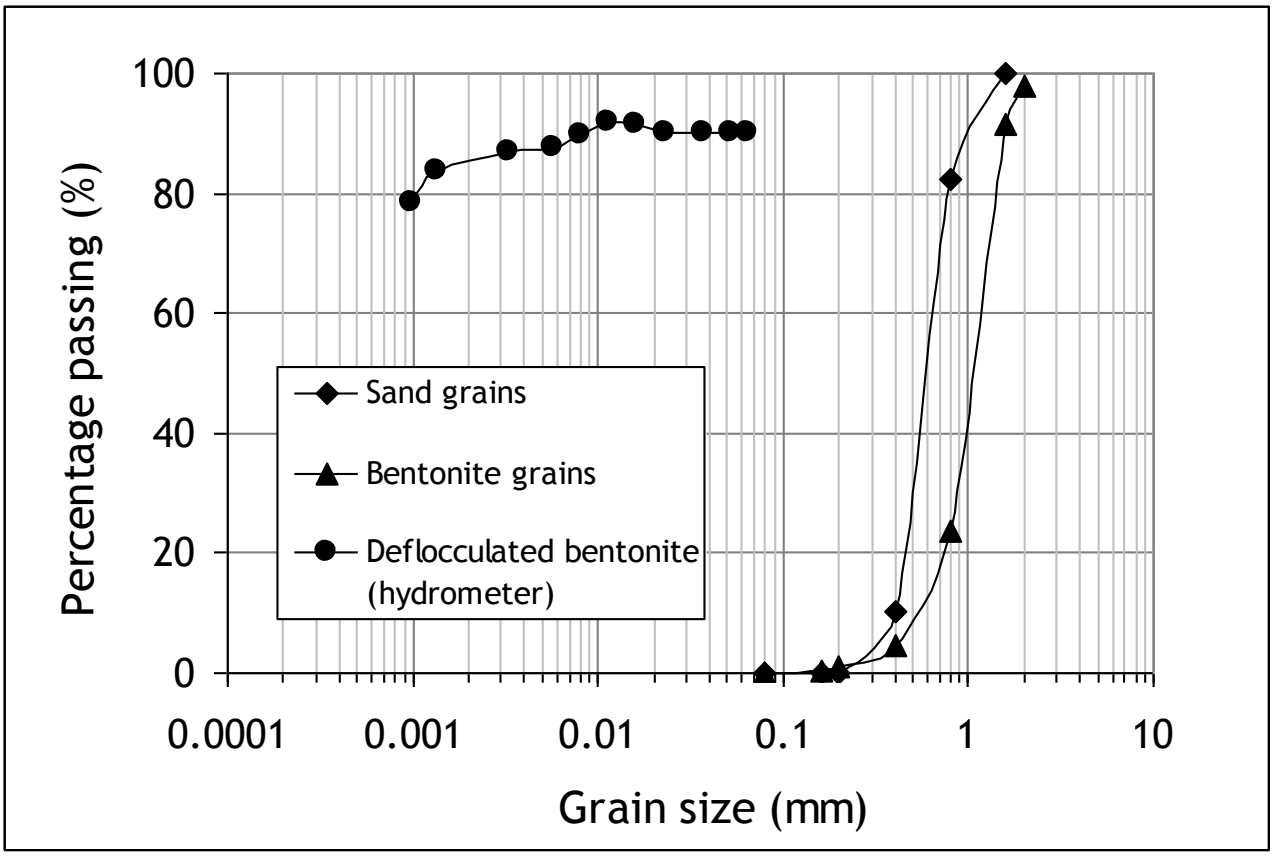

Figure 1. Grain size distribution curves.

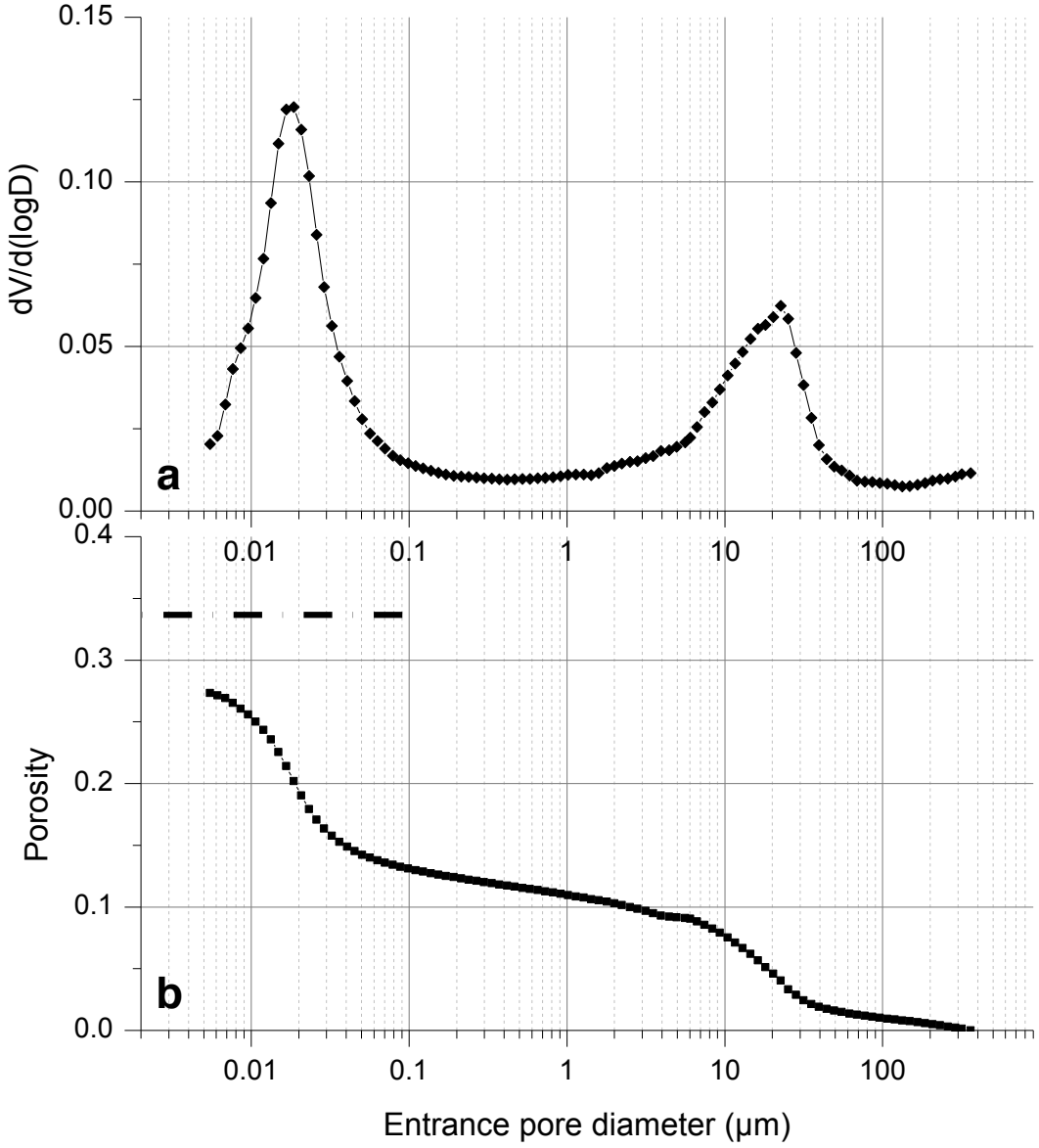

Figure 2. (a) Pore size distribution curve and (b) Cumulative porosity curve.

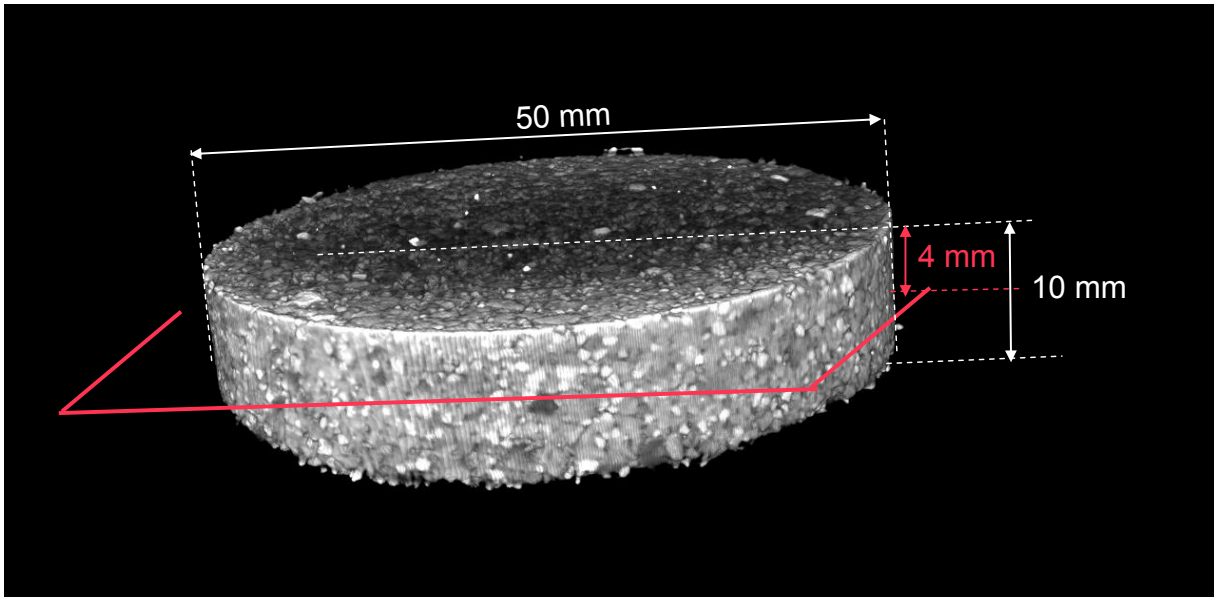

Figure 3. The 3D reconstructed image of the sample with the position of the cross section considered.

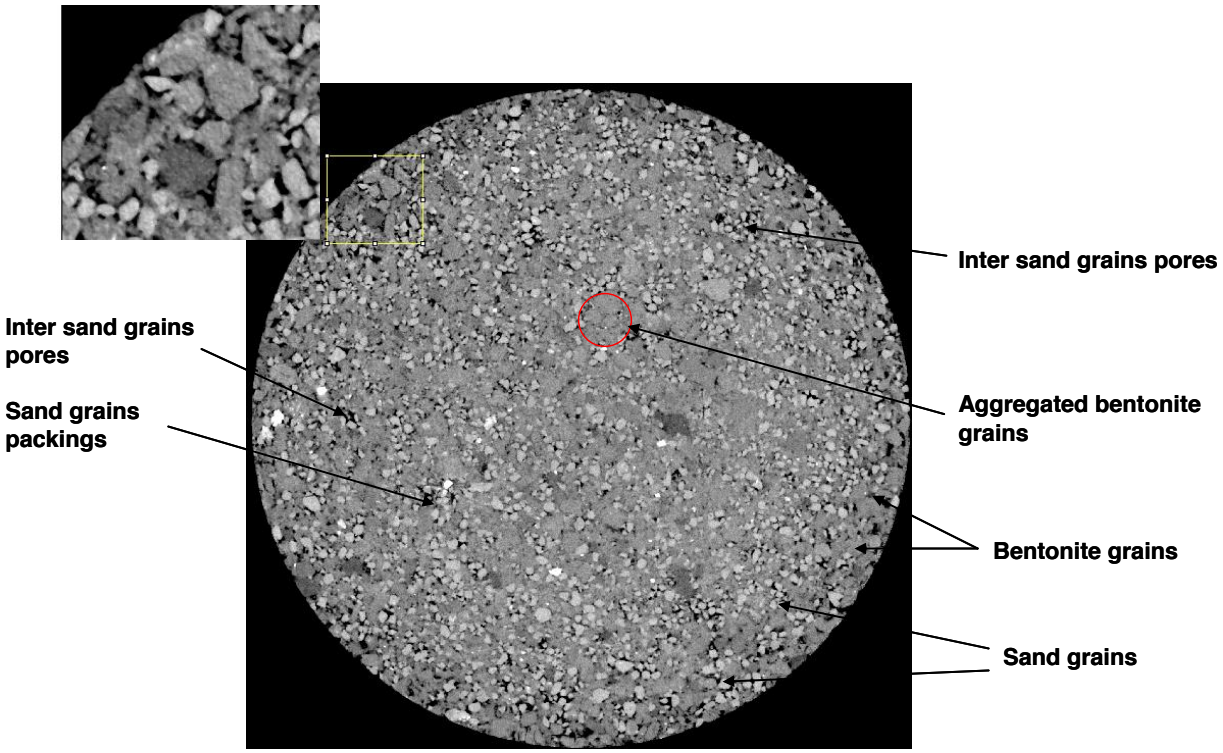

Figure 4. A typical horizontal μCT cross section of the compacted bentonite/sand mixture sample (dry density: 1.8 Mg/m^3, water content: 10%. disk diameter is 50 mm).

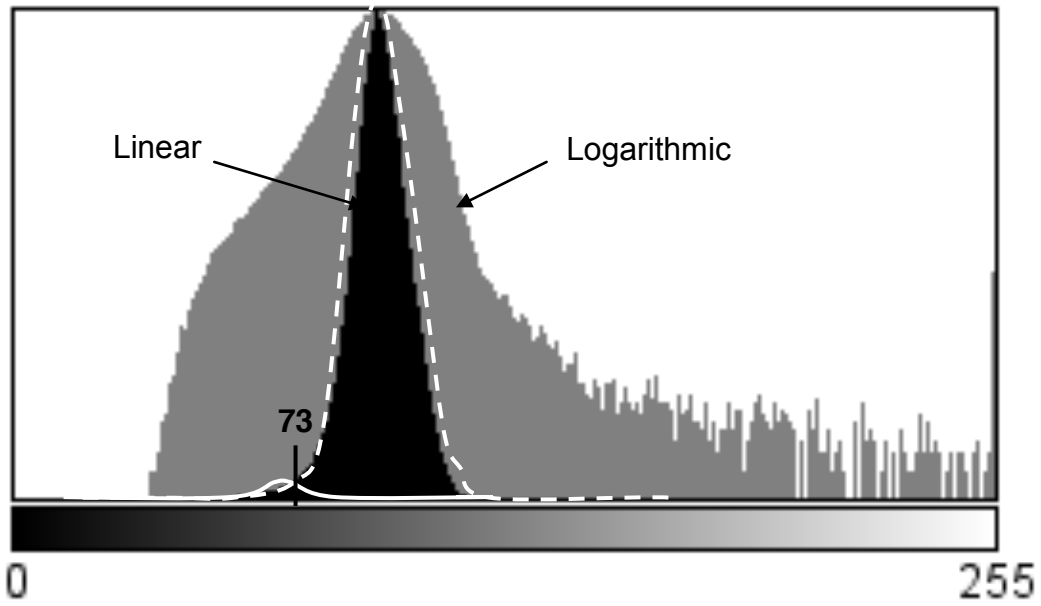

Figure 5. Histogram of the image (linear and logarithmic scale) with the fitted Gaussians and the obtained threshold value.

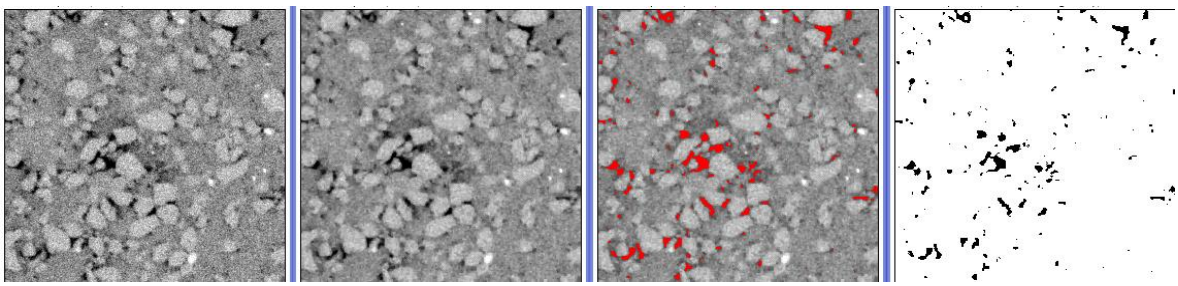

a) b) c) d)

Figure 6. Images at different stages before segmentation: a) non-treated, b) after applying 3D median filter, c) during threshold and d) final segmented image.

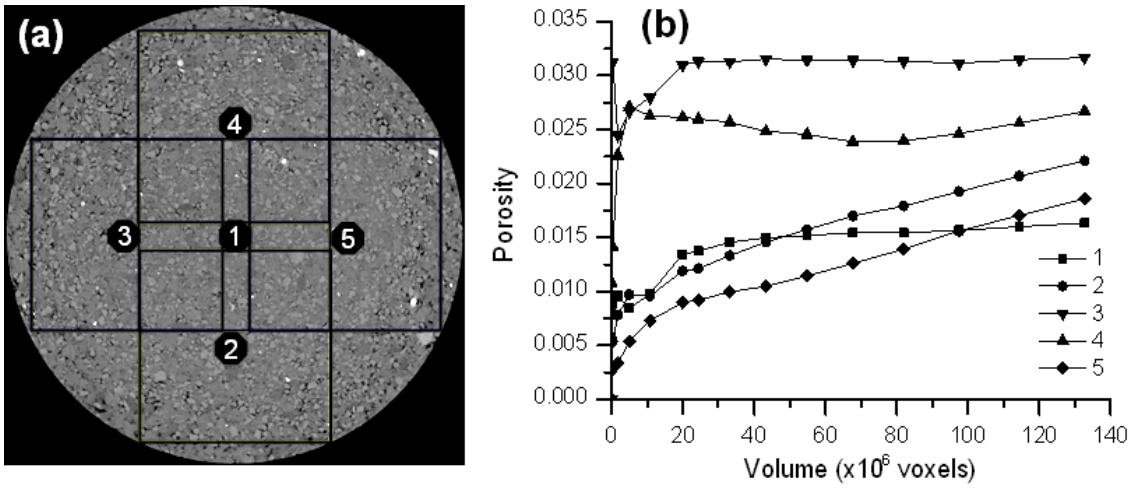

Figure 7. Calculated porosity for different volumes and at different locations in the sample.

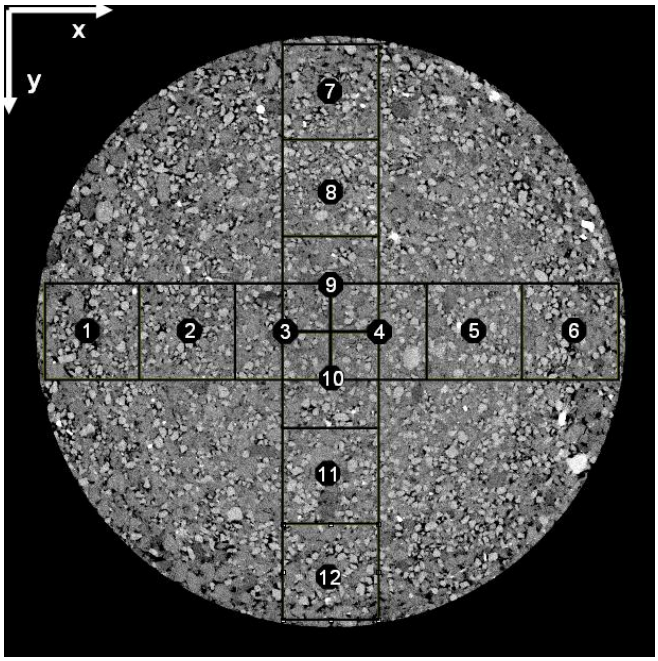

Figure 8. Sections of the volumes investigated in the sample (thickness 271 voxels).

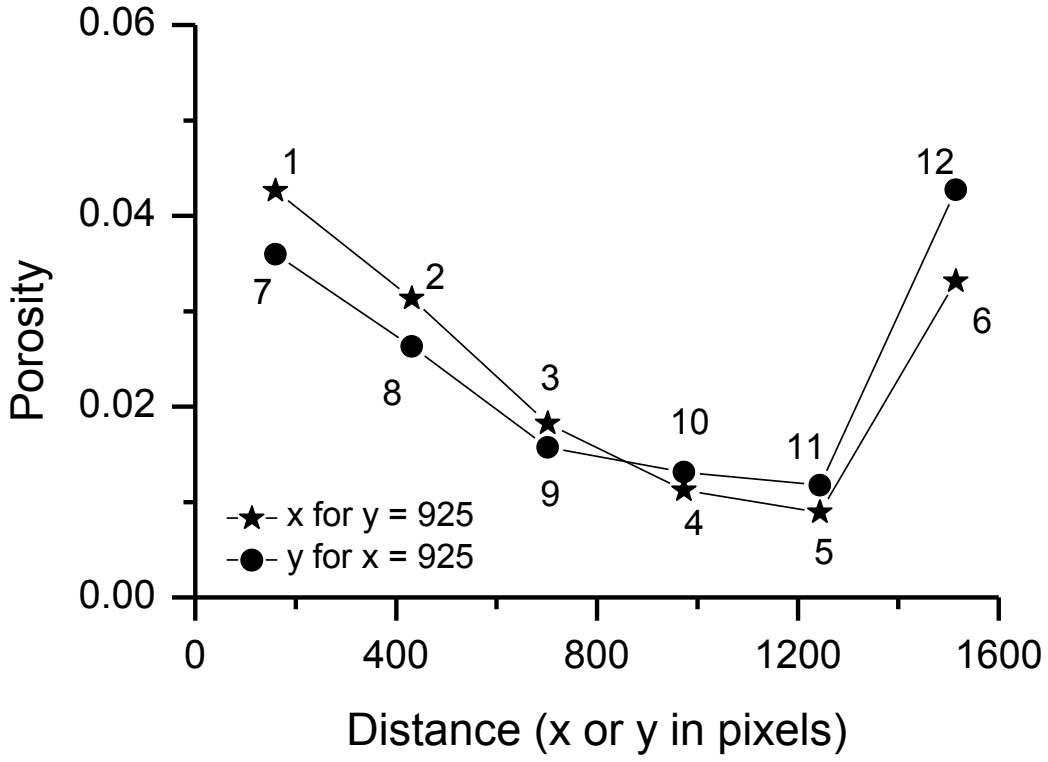

Figure 9. Porosity changes with respect to the position of the studied volume in the sample (x and y).

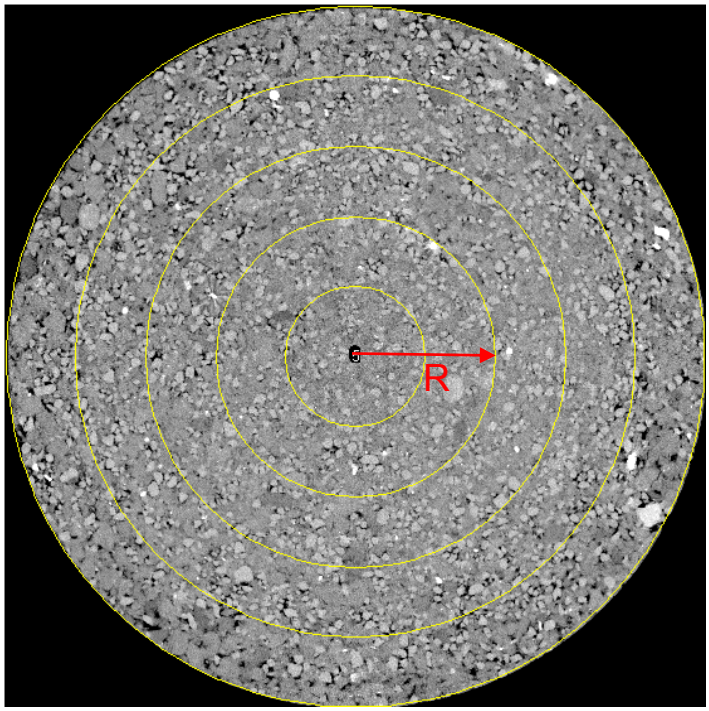

Figure 10. Concentric rings studied.

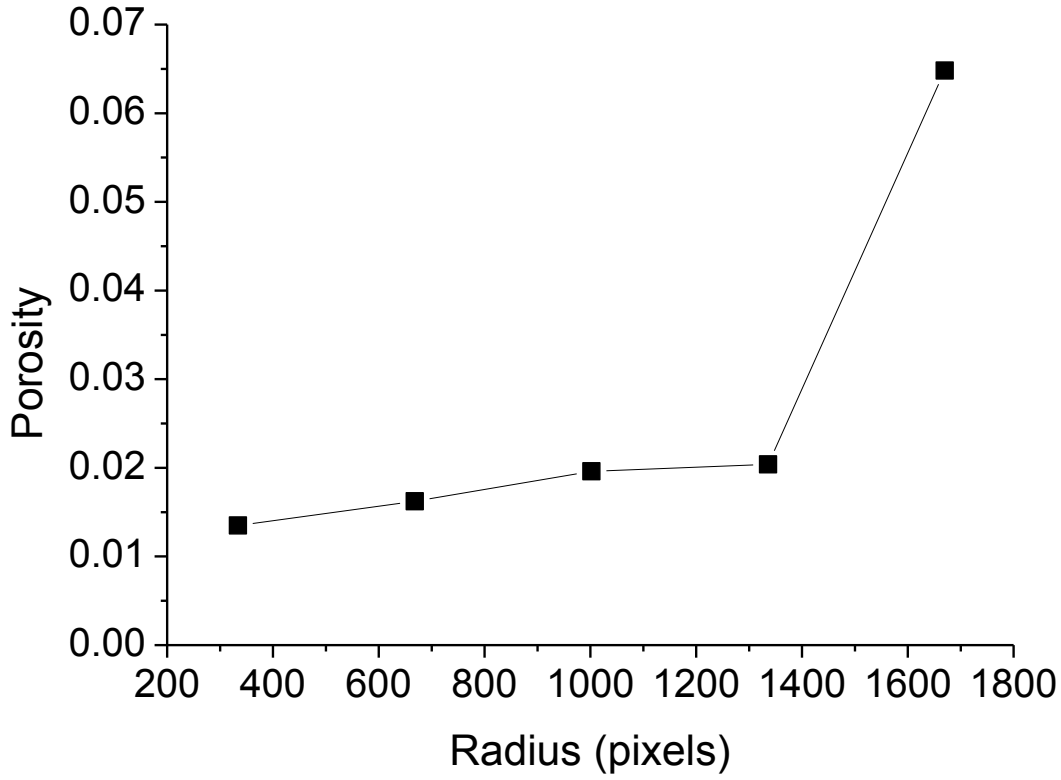

Figure 11. Changes in macro porosity with respect to the radius of the ring selected.